Word Count: 3535

Revision 2

Micro- structural and compositional evolutions during transformation from biotite to berthierine: Implications for phyllosilicates alteration process

JIAXIN XI[1,2,3], YIPING YANG[1,2], HONGPING HE[1,2,3*], HAIYANG XIAN[1,2], WEI TAN[1,2], RUI LI[4], JIANXI ZHU[1,2,3], HUIFANG XU[5]

[1] CAS Key Laboratory of Mineralogy and Metallogeny / Guangdong Provincial Key Laboratory of Mineral Physics and Materials, Guangzhou Institute of Geochemistry, Chinese Academy of Sciences, Guangzhou 510640, China

[2] CAS Center for Excellence in Deep Earth Science, Guangzhou 510640, China

[3] University of Chinese Academy of Sciences, Beijing 100049, China

[4] Center for Lunar and Planetary Sciences, Institute of Geochemistry, Chinese Academy of Sciences, Guiyang 550081, China

[5] Department of Geoscience, University of Wisconsin-Madison, 1215 West Dayton Street, Madison, Wisconsin 53706, USA

*Correspondence to: H.P. He (hphe@gig.ac.cn)

ABSTRACT

The composition and microstructure of phyllosilicates are prone to transformation due to their great sensitivity to surrounding physicochemical changes. Berthierine [$(R^{2+}, R^{3+},\square)_6(Si, Al)_4O_{10}(OH)_8$] ($\square$ represents octahedral vacancy) is a typical ferromagnesian phyllosilicate that commonly occurs in ferruginous rocks of shallow-marine habitats and has been used as an indicator of local depositional and/or hydrothermal activity in marine environments. However, little is known about the formation and mineralogy of nonmarine berthierine, particularly in volcanic systems. Using high-angle annular dark-field scanning transmission electron microscopy (HAADF–STEM), we have identified a berthierine twin structure within weakly altered biotite in a rhyolite from Long Valley, California, USA. The presence of nanoscale Fe-rich layers in the host biotite is revealed by energy-dispersive spectroscopy and electron energy loss spectroscopy (EELS). The HAADF–STEM pictures with atomic resolution demonstrate that the Fe-rich layers are composed of twinning berthierine layers rather than a single chlorite layer. The transformation of biotite to berthierine requires the dissolution of a tetrahedral (T) layer and the introduction of a new TO (O represents octahedral sheet) structure into the biotite stacking sequence, resulting in substituting one biotite layer (i.e., TOT) with two twinning berthierine layers (i.e., TO-OT). Observations based on morphology indicate that the transformation began at the biotite defect locations (such as screw dislocation, edge dislocation, and microcleavage fracture), concurrent with the rearrangement of metal cations. During the fluid alteration of biotite, berthierine was produced via an

interface-coupled dissolution-reprecipitation process. The EELS analyses further demonstrate that the Fe-rich biotite promotes the production of berthierine as the principal alteration product in low-temperature environments. Additionally, this study suggests that the combination of HAADF–STEM and EELS is effective for identifying nanominerals and elucidating their formation and alteration mechanisms.

Keywords: HAADF–STEM, EELS, biotite, berthierine twin, alteration mechanism

INTRODUCTION

Berthierine is a ferromagnesian phyllosilicate with a 1:1 layer structure like lizardite (Bailey 1988; Xu and Veblen, 1996). Similar to chlorite, berthierine has a stacking sequence of alternating tetrahedral and octahedral sheets with a stoichiometry of $[(R^{2+}, R^{3+},\square)_6(Si, Al)_4O_{10}(OH)_8]$ (Bailey and Brown 1962; Longstaffe 2003), in which Fe^{2+} is the primary octahedral cation, with flexible substitution of Fe^{3+}, Mg^{2+}, and Al^{3+} for Fe^{2+} (Guggenheim et al. 2006). Berthierine, frequently found in modern tropical shallow-marine sediments, is generated either by the direct precipitation from seawater or by the transformation of kaolinite and goethite (Porrenga 1965; Kodama and Foscolos 1981; Iijima and Matsumoto 1982; Edward et al. 1996; Wise 2007). Note that berthierine is also found in nonmarine environments, such as Arctic desert soils (Kodama and Foscolos 1981), coal swamps (Iijima and Matsumoto 1982), laterite belts (Toth and Fritz 1997), volcanic massive sulfide deposits (Slack et al. 1992), floodplains (Hornibrook and Longstaffe 1996), delta sediments (Taylor 1990), granite pegmatite (Wise 2007), metamorphic rocks

(Slack et al. 1992; Xu and Veblen 1996), and extrusive rocks (Li et al. 2014 and reference therein).

Berthierine is commonly regarded as a local indicator of marine environmental change (e.g., Houten and Purucker 1984; Huggett et al. 2010). Accordingly, its specific microstructure, which is sensitive to changes in temperature, burial depth, water content, and ion (e.g., Si and Fe cations) concentration in its formation environments, has received considerable attention (Li et al. 2014 and reference therein). Previous studies show that Al-rich phyllosilicates, such as kaolinite (Iijima and Matsumoto 1982), muscovite (Slack et al. 1992), illite (Sheldon and Retallack 2003), glauconite (Mu et al. 2015), and aluminosilicate glasses (Lee and Chatzitheodoridis 2016), can be converted to berthierine via hydrothermal activity with additional Fe ions. Conventionally, nonmarine berthierine is proposed to form below ~160 °C, corresponding to a burial depth of less than ~2.5 km (Li et al. 2014), in good agreement with the calculations based on the thermodynamic data of chamosite and berthierine (Xu 1993). Changes in environmental conditions can cause berthierine to additionally transform into interstratified chamosite/berthierine phases, and then (Fe-) chlorite (e.g., Xu et al. 1993; 1996).

Although nonmarine berthierine is a potential environmental indicator of volcanogenic sedimentary and late metamorphic processes of volcanic rocks (Sheldon and Retallack, 2003; Li et al. 2014), little is known about its production process and the mechanism involved (Li et al. 2014). Nonmarine berthierine has a complicated structure and composition comparable to other serpentine-group minerals; as a result,

it is frequently confused with chamosite or serpentine (Brindley 1968; Longstaffe 2003; Li et al. 2014). Traditional investigation techniques, such as powder X–ray diffraction and scanning electron microscope (SEM), cannot identify phyllosilicate species with sufficient precision due to their low resolution. In addition, the instability of berthierine under a focused electron beam, as well as the dynamic diffraction effects of parallel electron beams (Amouric et al. 1981; Olivés Baños and Amouric 1984), makes it difficult to obtain atomic-scale structural and compositional information using transmission electron microscopy (TEM) in order to distinguish berthierine from chamosite/serpentine.

The high-angle annular dark-field scanning transmission electron microscope (HAADF–STEM) can provide an image of crystals with incoherent atomic resolution (Pennycook 2002; Xu et al. 2016). Meanwhile, HAADF–STEM images will effectively simplify the location of atom column positions, resulting in an approximately twofold improvement in resolution over high-resolution TEM images (Xu et al. 2014; Yang et al. 2021). Without the effect of crystal thickness on image contrast (Pennycook, 2002), the intensity of atom columns can directly reflect their mean atomic number (Z), which can be used to determine the crystal structures of nanominerals (Xu et al. 2014; 2015; 2016; Xi et al. 2022; Yang et al. 2022a, b). Additionally, electron energy loss spectroscopy (EELS) can provide an atomic-scale composition and redox state information with energy resolutions as low as 1 eV (Garvie et al. 1994; Garvie and Buseck 1998; Xu 2000; Aken et al. 2002).

Thus, we used a combination of HAADF–STEM and EELS to investigate

105 berthierine in a weakly altered biotite phenocryst of rhyolite from Long Valley,
106 California, USA (Varga et al., 1990; Christensen and Depaolo, 1993). Weakly altered
107 biotite preserves nanoscale alteration rims recording microstructural and
108 compositional evolution processes very well. Our study reveals that a high iron
109 content considerably influences the biotite transformation pathway and facilitates the
110 formation of berthierine in a low-temperature environment. This is the first report
111 about the formation of nanoscale interstratified twinning berthierine layers in biotite,
112 shedding light on the biotite-to-berthierine transformation process.
113

114 **SAMPLE DESCRIPTION AND EXPERIMENTAL METHODS**

115 The biotite samples were recovered from rhyolite in the Long Valley Caldera,
116 California, USA. The Long Valley magmatic system is distributed east of the Sierra
117 Nevada along the western edge of the Basin and Range Province (Fig. 1) (Metz and
118 Mahood, 1991). The caldera remains thermally active, with numerous hot springs and
119 fumaroles, and has undergone considerable deformation due to earthquakes and other
120 disturbances. A major explosive eruption at 0.73 Ma formed the caldera with the
121 basalt that is referred to the precaldera high-silica rhyolite lava. Biotite is the
122 predominant mafic phenocryst in the lavas and ash-fall deposits of the magmatic
123 system (Fig. 2a-b) (Metz and Mahood 1991). These xenocrystal biotite particles
124 produced from the depths show euhedral morphology (Andersson and Eklund 1994;
125 Ginibre et al. 2002). Isotopic analyses and mineralogical observations reveal a low
126 degree of alteration in samples collected from the same area, as evidenced by the

absence of bulk quantities of alteration products (Varga et al. 1990; Metz and Mahood 1991; Christensen and Depaolo 1993). Optical microscopy (Fig. 2a–b) and SEM analyses reveal thin altered rims at the boundaries of biotite and kaersutite (Fig. S1a–c) (Fig. 3a–c); (Andersson and Eklund 1994; Ginibre et al. 2002). To display various mineral species, a polarizing filter combined with a lambda compensator was used, which made the displayed-color different from the original interference colors of minerals. These observations demonstrate that the majority of mineral phenocrysts, including biotite and kaersutite, have thin altered rims at the grain boundaries (Fig. S1a–c).

The chemical composition of biotite was determined using a JEOL JXA-8230 electron probe microanalyzer (EPMA) (Japan). In addition, the ZAF correction method was used for data reduction. Standard materials used for data correction were provided by Structure Probe, Inc., (SPI) Supplies (United States), with orthoclase for K, albite for Na, BaF_2 for F, chrome-diopside for Si and Ca, olivine for Mg, magnetite for Fe, rutile for Ti, rhodonite for Mn, and pure aluminum metal for Al. The average formula of biotite was calculated according to the electron probe microanalysis, which is as follows:

$$(K_{0.89}Na_{0.08})_{\sum=0.97}(Fe_{1.61}Ti_{0.27}Mg_{0.95}Mn_{0.03})_{\sum=2.86}(Si_{2.84}Al_{1.16})_{\sum=4.00}O_{10}[F_{0.08}Cl_{0.02}(OH)_{1.90}]_{\sum=2.00}.$$

An FEI Scios Dual-beam system was utilized to obtain SEM images and focused ion beam (FIB) cross-sections (ThermoFisher Scientific, United States). Thin sections cut from the edge of the biotite particle (marked by the yellow frame in Figs. 3e and

S1d, e) using FIB were used to investigate the alteration structure at the boundary of the biotite phenocrysts. STEM, energy-dispersive X-ray spectroscopy (EDS), and EELS experiments were then conducted at 200 kV voltage using an FEI Talos F200S field-emission transmission electron microscope (ThermoFisher Scientific, United States). The TEM is coupled with a HAADF detector, two Super X high-resolution energy-dispersive spectrometers, and a Gatan 1077 EELS spectrometer. Z-contrast images were taken using a camera length of 160 mm to maximize the contrast variations between the different atoms in the HAADF images (Xu et al. 2014, 2015). A Gatan Digital Micrograph (version 3.50) was used to remove the contrast noise induced by the amorphous materials in the HAADF–STEM images, generate EELS mapping images with background correction, and perform data fitting. The semi-quantitative EDS analytical lines were as follows: Na-K_α, Mg-K_α, Al-K_α, Si-K_α, K-K_α, Ti-K_α, Mn-K_α, and Fe-K_α. For comparison, the intensities of Si (Kα) peaks at ~1.75 keV (Fig. 6b-c) were retained to be equivalent. Notably, the O content computed from the stoichiometry of cations in the sample differed from the actual value in the EDS data.

PHASE OBSERVATION AND IDENTIFICATION

Morphology observation

The SEM (Fig. 3d) and TEM (Fig. 4a) images show that biotite and adjacent plagioclase are separated by a ~50-nm wide crack that was filled with secondary clay minerals with an irregular morphology (black arrow in Fig. 4b), indicating the

171 presence of weak alteration at the edge of biotite particles. The enlarged STEM image
172 reveals that interlayer defects (indicated by the yellow arrows in Fig. 4c) paralleling
173 the basal plane of the host biotite exhibit different contrasts than the well-crystallized
174 host biotite.

175 The two-dimensional TEM lattice fringes (Fig. 5a-b) and selected-area electron
176 diffraction (SAED) patterns produced from well-crystallized and interlayer defect
177 zones in the biotite along the [110] zone axis display distinctive characteristics (Figs.
178 4a and 5b, insets). The sharp and bright diffraction spots in the SAED pattern (Fig. 4a,
179 inset) suggest that the well-crystallized host biotite possesses a 1*M* structure (regions
180 A and C in Fig. 5a). In contrast, the interlayer defect domain shows a fast Fourier
181 transform (FFT) pattern with streaking and diffusion feature in the *hkl* ($k \neq 3n$, n is
182 an integer) rows along the [001] zone axis (Fig. 5b, inset). The corresponding TEM
183 images (Figs. 4c and 5a-b) show distinct contrast regions within the host 1*M* biotite
184 (marked by the yellow arrows in Figs. 4c and 5a–b), while the interlayer defect
185 domains and the well-crystallized host biotite had a similar crystallographic
186 orientation (i.e., the [001] zone axis).

187 **Compositional analysis**

188 The EDS spectra obtained from well-crystallized and interlayer defect domains
189 (Fig. 6a) exhibit distinct K, Mg, Al, and Fe signal intensities (Fig. 6b and c). Notably, a
190 significant enrichment of Fe is evident in the bright zone (Fig. 6b), whereas practically
191 all metal cations, mainly Fe and K, exhibited a low signal intensity in the deeper layers
192 (Fig. 6c).

193 In addition, the EELS mapping reveals a considerable enrichment of Fe in the
194 high-contrast areas (Fig. 7a–b). Furthermore, the electron energy loss near-edge
195 structure (ELNES) of the Fe $L_{3,2}$-edges reveals different valence states of Fe in the
196 well-crystallized biotite domain (i.e., the dark domain, frame 1 in Fig. 7b) and the
197 interlayer defect domains (i.e., bright domain, frame 2 in Fig. 7b). After being
198 normalized according to the intensity of the Fe-L_3 edge, the bands at 705–730 eV (Fig.
199 7c) exhibit distinct shapes and energy shift. In addition, the spectral peaks of frame 2
200 (the red line in Fig. 7c) have lower energy than those of frame 1 (the black line in Fig.
201 7c). Moreover, the spectra of well-crystallized biotite exhibit a single peak at 710.06
202 eV, but the spectrum of the interlayer defect exhibits a poorly resolved doublet with
203 peaks at 709.67 and 711.22 eV, respectively. Notably, the valence state of Fe affects the
204 ELNES characteristics of the Fe $L_{3,2}$ edges (e.g., Xu 2000; Aken and Liebscher 2002).
205 The discrepancy in Fe-$L_{3,2}$ ELNES suggests that the valence states of Fe in defective
206 domains and biotite areas are distinct. Accordingly, the ratios can be obtained using the
207 integral signals at 708.85–710.95 and 719.65–721.75 eV in the EELS spectra after
208 background subtraction from the Fe $L_{3,2}$-edges (Garvie and Buseck 1998; Aken et al.
209 1998; Aken and Liebscher 2002). According to our calculations, well-crystallized
210 biotite has ~30% Fe^{3+} and ~70% Fe^{2+}, whereas interlayer defect domains consist of
211 ~40% Fe^{3+} and ~60% Fe^{2+}.

212 According to EELS and EDS analyses, the average chemical formula of the
213 interlayer defect domains is $[Fe^{2+}_{1.82}Fe^{3+}_{1.20}Mg_{1.09}Al_{0.65}Ti_{0.30}]_{\sum=5.06}[Si_{3.26}Al_{0.74}]_{\sum=}$
214 $_{4.00}O_{18}$, whereas the EDS values were calibrated using the composition of the host

biotite as determined by EPMA. Although iron cations typically occupy the octahedral positions in phyllosilicates, we find that Fe^{2+} continues to be the predominant octahedral cation in these interlayer defect domains.

HAADF–STEM observation

Bright (or dark) lines in a HAADF image with Z contrast indicate phases composed of elements with high (or low) atomic numbers. The SAED pattern (Fig. 5b) and HAADF–STEM images (Fig. 8) demonstrate that the interlayer defect domains and the well-crystallized 1*M* biotite host have a common crystallographic orientation along the [001] zone axis. Due to the relatively high contents of Fe and Ti in biotite, all the bright lines are classified as octahedral (O) sheets, and the separated spots sandwiched by O sheets are interlayer K^+. The tetrahedral (T) sheets adjacent to the O sheets are connected to the K^+ plane, and the spots indicating atoms in the T sheets are invisible due to their low contrast and resolution limit (Fig. 8). Consequently, the interlayer defect domains are characterized by two bright O sheets with a ~4 Å spacing sandwiched by TOT layers (Fig. 8b). In conjunction with compositional analyses, these interstratified layers are identified as two berthierine-like layers with TO-type structure (red arrows in Fig. 8c). These TO units are paired, forming a structure with mirror-symmetry that parallels the basal plane of biotite (Fig. 8b). When the berthierine twin structure develops in pairs, a Z-shaped structure is likely to form (Fig. 9a–b). In this instance, the transformation from biotite (Fig. 9c) to berthierine twin layers terminated at the contact of the paired berthierine twin structure (Fig. 9d), leading to the formation of a jagged joint in the Z-shaped structure

(Fig. 9b–d). These interstratified layers are brighter than the host biotite layers, suggesting their higher Fe content.

DISCUSSION

Identification of berthierine interstratification

Biotite has a stacking sequence of TOT-K with ~10 Å lattice spacing (Fig. 9c), (e.g., Veblen and Ferry 1983; Xu et al. 1996). Chlorite has a TOT-O structure and ~14 Å lattice spacing (Fig. 9e), while berthierine has a TO structure and ~7 Å lattice spacing (Fig. 9d) (Lee and Peacor 1985; Bailey 1988). Biotite is typically transformed into chlorite in the majority of natural occurrences (e.g., Veblen and Ferry 1983; Xu et al. 1996). Previous studies have established two models for transforming biotite into phyllosilicate minerals of the TOT-O type. The model 2TOT→1TOTO, which proposes the conversion of two biotite layers into one TOT-O layer by forming an O sheet and removing the two T sheets of one TOT biotite layer (e.g., Eggleton and Banfield 1985; Xiao and Chen 2020), is widely accepted as the mechanism of biotite chloritization. And the 1TOT→1TOTO model, creating an extra O sheet in the interlayer region between two TOT layers of biotite, has been proposed to be unlikely according to the investigations of chlorite in numerous igneous and metamorphic rocks (e.g., Veblen 1983; Veblen and Ferry 1983). In particular, the present study demonstrates a new route of biotite-to-berthierine transformation via the 1TOT→2TO (twinning) mechanism. The alteration begins with the formation of interstratified berthierine monolayers at biotite defects, followed by the transformation of a biotite

259 TOT layer into two TO layers (TO-OT) of berthierine.

260 The presence of ~4 Å spacing between two octahedral sheets in the HAADF–
261 STEM images of biotite is the key evidence for distinguishing the twinning
262 berthierine layers from a single chlorite layer (Figs. 9b and 10a). If the replacement of
263 interlayer K^+ by a newly formed brucite-like O sheet leads to the formation of TOT-O
264 structure (Fig. S3b) as described in the model proposed by Wang et al. (2019), the
265 stacking sequence in altered products would change from the original TO_1T-K-TO_2T
266 to TO_1T-O_3-TO_2T (1, 2, and 3 denote three different octahedral sheets), and the newly
267 formed O_3 sheet would be equidistant to O_1 and O_2 (Fig. S3b). The spacing between
268 O_1 and O_3 should be ~7 Å, the same as that between O_2 and O_3 (Fig. 9e). Note that the
269 STEM images show that the spacing between adjacent O sheets in the interlayer
270 defect domains is ~4 Å, whereas the distance between adjacent O sheets in biotite is
271 ~10 Å (Figs. 8b and 9b). The presence of ~4 Å spacing demonstrates that the twining
272 layer of berthierine in the modification product has a TO-OT stacking pattern.

273

274 **Formation mechanism of berthierine structure in biotite**

275 The present study demonstrates that berthierine can form at the nanoscale level
276 in the rhyolite of the Long Valley Caldera, although berthierine has yet to be widely
277 observed there. Previous studies have proved that annite (i.e., the end member of
278 biotite with Fe cations occupying all octahedral sites) can transform to berthierine in
279 an environment with a high activity ratio of $a(Fe^{2+})/a(H^+)$ and $a(Fe^{2+})/a(Mg^{2+})$ (Xu
280 1993; Li et al. 2014). It is hypothesized that the Fe content is a crucial element

determining the activity and transformation products of biotite during its transformation into berthierine. Chemical analysis suggests that the studied biotite $\{(K_{0.89}Na_{0.08})_{\sum=0.97}($ $Fe^{2+}_{1.13}Fe^{3+}_{0.48}$ $Ti_{0.27}Mg_{0.95}Mn_{0.03})_{\sum=2.86}(Si_{2.84}Al_{1.16})_{\sum=4.00}O_{10}[F_{0.08}Cl_{0.02}(OH)_{1.90}]_{\sum=2.00}\}$ is enriched in Fe, with ~51% mole fraction of annite ($[KFe_3(AlSi_3O_{10})(OH)_2]$) (Guggenheim et al. 2007). Consequently, high proportions of Fe can be released during the dissolution of the host biotite, which significantly increases the ratios of $a(Fe^{2+})/a(H^+)$ and $a(Fe^{2+})/a(Mg^{2+})$ in an ambient environment, facilitating the formation of berthierine as an alteration product of the studied biotite. In addition, thermodynamic studies have placed the stable temperature range of berthierine between 40 and 120 °C (Nelson and Roy 1958; Bostick 1978; Ahn and Peacor 1985; Hillier and Velde 1992; Mosser-Ruck et al. 2010), while berthierine transforms into chlorite at 160–190 °C or a burial depth of >2.5 km (Iijima and Matsumoto 1982; Xu 1993; Bertoldi et al. 2007). The low formation temperature of berthierine is consistent with the fact that the alteration of biotite occurs near the surface following the eruption of local rhyolitic magma and the diagenesis of rhyolite (Varga et al. 1990). Hence, this study suggests that a high Fe concentration in biotite and a near-surface alteration environment favor the transformation of biotite-to-berthierine over chlorite.

The transformation from biotite to berthierine twinning layers most likely occurred via an interface-coupled dissolution-reprecipitation process (Figs. 10b and 11). This process can achieve complete structural and chemical reorganization only with a slight modification of the parent structure via cation and anion exchange

(Putnis 2009). Similar solid-solid transformation processes have been suggested by some studies, such as the transformation from the serpentine structure to the chlorite structure by shifting Si and H atoms (Xu and Veblen 1996), and the formation of hydroxyapatite structure via the Cl-ion exchange in the calcium and strontium chlorapatite crystals (Yanagisawa et al. 1999). Our HR(S)TEM observations show that the two mirror-symmetry TO layers in the berthierine twinning structure and the TOT-K layers in the host biotite of 1*M* polytope share the same crystallographic orientation (Fig. 8b). This suggests that the newly formed berthierine inherits the crystallographic orientation of dissolved biotite throughout the transformation (Figs. 4b and 8b). At the onset of biotite transformation, defects (Fig. 11a) such as dislocations and microcleavage planes (indicated by the yellow triangles in Fig. 10a), with a flexible structure and relatively high surface energy, initiate the transformation (e.g., Min, 1992; Lu et al., 2016). Meanwhile, interlayer ions K^+ and Si in exposed Si–O tetrahedra are readily released during alteration (Lu et al., 2016), which facilitates the dissolution of T sheets in defect-rich biotite (Kuwahara and Yaoki, 1995). The dissolution is accompanied or followed by the nucleation of berthierine at the defective planes of the parent biotite via cation rearrangement and structural matching (Putnis and Putnis 2007; Putnis 2009) (Fig. 11b). Due to the loss of cations in their O sheets, Fe-poor layers form, and the released cations reprecipitate as Fe-rich layers attached to the Fe-poor layers (Figs. 8a and 11b). The gradual alteration at the biotite-berthierine interface may result in the complete transformation of biotite into berthierine.

IMPLICATION

As an evolution product of phyllosilicates, secondary berthierine is a potential indicator of surrounding environments, such as temperature, oxygen fugacity, and redox state of late alteration in local extrusive rocks. Berthierine is often less stable than chlorite on/near the surface (Blanc et al. 2015), although it may be the major alteration product of Fe-rich phyllosilicates in moist environments at a shallow burial depth (<1.6 km) and low temperature (<160 °C) (e.g., Wilson et al. 2006). Given that berthierine can be easily confused with chamosite or serpentine (Brindley 1968; Longstaffe 2003; Li et al. 2014), the present study implies that berthierine may be a common phase as alteration product of Fe rich biotite when carefully investigated with HAADF-STEM and EELS.

It is believed that an interface-coupled dissolution-reprecipitation process (Putnis 2009) in a solvent-mediated environment dominates the biotite-to-berthierine transformation mechanism. Defect areas in the original biotite provide high-energy planes that facilitate reactions, including the dissolution of exposed T sheets, reprecipitation of new O sheets, and nucleation of berthierine twin structures. The novel microstructural evidence sheds new light on the evolution of 2:1-type to 1:1-type phyllosilicate minerals during mineral-fluid reactions that may have occurred during metasomatism and weathering processes. Such transformation mechanism may be also involved in other minerals' transformation processes, such as the replacement of serpentine minerals by chlorite and the conversion from chlorapatite to

hydroxyapatite.

This study demonstrates that HAADF–STEM is a more effective approach than XRD and TEM for in situ identifying alteration products. With the help of lattice spacing determination, contrast comparison of HAADF–STEM images, and high-resolution EELS spectra, we successfully depicted the atomic arrangements of biotite and the interface texture between the berthierine twin structure and host biotite. Accordingly, we argue that those cutting-edge techniques (e.g., HAADF–STEM and EELS) with high spatial and energy resolutions are highly important for disclosing clay minerals' structures at the nanoscale, and can be extended to other minerals and materials with complicated microstructure and related phase transformation.

ACKNOWLEDGMENTS

This work was financially supported by the National Natural Science Foundation of China (Grant Nos. 41921003, 41825003, and 42072044) and Science and Technology Planning Project of Guangdong Province, China (2020B1212060055).

REFERENCES

Ahn, J.H., and Peacor, D.R. (1985) Transmission electron microscopic study of diagenetis chlorite in Gulf Coast argillaceous sediments. Clays and Clay Minerals, 33, 228–236.

Amouric, M., Mercuriot, G., and Baronnet, A. (1981) On computed and observed HRTEM images of perfect mica polytypes. Bulletin de Minéralogie, 104, 298–313.

Andersson, U.B., and Eklund, O. (1994) Cellular plagioclase intergrowths as a result of crystal-magma mixing in the Proterozoic Åland rapakivi batholith, SW Finland. Contributions to Mineralogy and Petrology, 117, 124–136.

Bailey, R.A., Dalrymple, G.B., and Lanphere, M.A. (1976) Volcanism, structure, and geochronology of Long Valley caldera, Mono County, California. Journal of Geophysical Research, 81, 725–744.

Bailey, S.W. (1988) X-ray diffraction identification of the polytypes of mica, serpentine, and chlorite. Clays and Clay Minerals, 36, 193–213.

Bailey, S.W., and Brown, B.E. (1962) Chlorite polytypism: I. Regular and semi random one-layer structures. American Mineralogist, 47, 819–850.

Bertoldi, C., Dachs, E., and Appel, P. (2007) Heat-pulse calorimetry measurements on natural chlorite-group minerals. American Mineralogist, 92, 553–559.

Blanc, P., Vieillard, P., Gailhanou, H., Gaboreau, S., Gaucher, E., Fialips, C.I., Made, B., and Giffaut, E. (2015) A generalized model for predicting the thermodynamic properties of clay minerals. American Journal of Science, 315, 734–780.

Bostick, N.H., Cashman, S.M., McCulloh, T.H., and Waddell, C.T. (1978) Gradients of vitrinite reflectance and present temperature in the Los Angeles and Ventura Basins, California. Pecific, section SEPM, 65–96.

Bourdelle, F., Benzerara, K., Beyssac, O., Cosmidis, J., Neuville, D.R., Brown, G.E., and Paineau, E. (2013) Quantification of the ferric/ferrous iron ratio in silicates by scanning transmission X-ray microscopy at the Fe $L_{2,3}$ edges. Contributions to Mineralogy and Petrology, 166, 423–434.

Brindley, G.W., Bailey, S.W., Faust, G.T., Forman, S.A., and Rich, C.I. (1968) Report of the nomenclature committee (1966–67) of the clay minerals society. Clays and Clay Minerals, 16, 322–324.

Cathelineau, M. (1988) Cation site occupancy in chlorites and illites as a function of temperature. Clay Minerals, 23, 471–485.

Chamberlain, K.J., Morgan, D.J., and Wilson, C.J.N. (2014) Timescales of mixing and mobilisation in the Bishop Tuff magma body: Perspectives from diffusion chronometry. Contributions to Mineralogy and Petrology, 168, 1–24.

Christensen, J.N., and Depaolo, D.J. (1993) Time scales of large volume silicic magma systems: Sr isotopic systematics of phenocrysts and glass from the Bishop Tuff, Long Valley, California. Contributions to Mineralogy and Petrology, 113, 100–114.

Dora, M.L., and Randive, K.R. (2015) Chloritisation along the Thanewasna shear zone, Western Bastar Craton, Central India: Its genetic linkage to Cu-Au mineralisation. Ore Geology Reviews, 70, 151–172.

Edward, E.R.C., Hornibrook, E.R.C., and Longstaffe, F.J. (1996) Berthierine from the Lower Cretaceous Clearwater Formation, Alberta, Canada. Clays and Clay Minerals, 44, 1–21.

Garvie, L.A.J., and Buseck, P.R. (1998) Ratios of ferrous to ferric iron from nanometre-sized areas in minerals. Nature, 396, 667–670.

Garvie, L.A.J., Craven, A.J., and Brydson, R. (1994) Use of electron energy-loss near-edge fine structures in the study of minerals. American Mineralogist, 79, 411–425.

Ginibre, C., Wörner, G., and Kronz, A. (2002) Minor- and trace-element zoning in plagioclase: Implications for magma chamber processes at Parinacota volcano, northern Chile. Contributions to Mineralogy and Petrology, 143, 300–315.

Guggenheim, S., Adams, J.M., Bain, D.C., Bergaya, F., Brigatti, M.F., Drits, V.A., Formoso, M.L.L., Galán, E., Kogure, T., and Stanjek, H. (2007) Summary of

420 recommendations of nomenclature committees relevant to clay mineralogy:
421 Report of the association internationale pour l'etude des argiles (AIPEA)
422 nomenclature committee for 2006. Clay Minerals, 42, 575–577.

423 Hillier, S., and Velde, B. (1992) Chlorite interstratified with a 7 Å Mineral: An
424 example from offshore Norway and possible implications for the interpretation
425 of the composition of diagenetic chlorites. Clay Minerals, 27, 475–486.

426 Hornibrook, E.R.C., and Longstaffe, F.J. (1996) Berthierine from the lower cretaceous
427 clearwater formation, Alberta, Canada. Clays and Clay Minerals, 44, 1–21.

428 Huggett, J.M., Gale, A.S., and Mccarty, D. (2010) Petrology and palaeoenvironmental
429 significance of authigenic iron-rich clays, carbonates and apatite in the Claiborne
430 Group, Middle Eocene, NE Texas. Sedimentary Geology, 228, 119–139.

431 Iijima, A., and Matsumoto, R. (1982) Berthierine and charosite in coal measures of
432 Japan. Clays and Clay Minerals, 30, 264–274.

433 Kodama, H., and Foscolos, A.E. (1981) Occurrence of berthierine Canadian Arctic
434 Desert soils. Cannadian Mineralogist, 19, 279–183.

435 Kuwahara, Y. (1995) Dissolution process of phlogopite in acid solutions. Clays and
436 Clay Minerals, 43, 39–50.

437 Lee, J.H. (1985) Ordered 1:1 interstratification of illite and chlorite: A transmission
438 and analytical electron microscopy study. Clays and Clay Minerals, 33, 463–467.

439 Lee, M.R., and Chatzitheodoridis, E. (2016) Replacement of glass in the Nakhla
440 meteorite by berthierine: Implications for understanding the origins of
441 aluminum-rich phyllosilicates on mars. Meteoritics and Planetary Science, 51,
442 1643–1653.

443 Li, X.G., Liu, Q.F., Cheng, H.F., Kang, Y.X., and Sun, B. (2014) Chemical
444 constituent,structure and formation environment of berthierine. Bulletin of
445 Mineralogy, Petrology and Geochemistry, 33, 116–123.

446 Longstaffe, F.J. (2003) Berthierine, 104 p. Springer, Berlin.

447 Lu, Y., Wang, R., Lu, X., Li, J., and Wang, T.T. (2016) Reprint of Genesis of
448 halloysite from the weathering of muscovite: Insights from microscopic
449 observations of a weathered granite in the gaoling region, Jingdezhen, China.
450 Applied Clay Science, 119, 59–66.

451 Metz, J.M., and Mahood, G.A. (1991) Development of the long valley, California,
452 magma chamber recorded in precaldera rhyolite lavas of glass mountain.
453 Contributions to Mineralogy and Petrology, 106, 379–397.

454 Min, N.B. (1992) Growth mechanisms in real crystals. Journal of Synthetic Crystals,
455 21, 217–229.

456 Mosser-Ruck, R., Cathelineau, M., Guillaume, D., Charpentier, D., Rousset, D.,
457 Barres, O., and Michau, N. (2010) Effects of temperature, pH, and iron/clay and
458 liquid/clay ratios on experimental conversion of dioctahedral smectite to
459 berthierine, chlorite, vermiculite, or saponite. Clays and Clay Minerals, 58, 280–
460 291.

461 Mu, N., Schulz, H.M., Fu, Y.J., Schovsbo, N.H., Wirth, R., Rhede, D., and van Berk,
462 W.V. (2015) Berthierine formation in reservoir rocks from the Siri oilfield
463 (Danish North Sea) as result of fluid-rock interactions: part I. Characterization.
464 Marine and Petroleum Geology, 65, 302–316.

465 Nelson, B.W., and Roy, R. (1958) Synthesis of the chlorites and their structural and
466 chemical constitution. American Mineralogist, 43, 07–725.

Olivés Baños, J., and Amouric, M. (1984) Biotite chloritization by interlayer brucitization as seen by HRTEM. American Mineralogist, 69, 869–871.

Pennycook, S.J. (2002) Structure determination through Z-contrast microscopy. Advances in Imaging and Electron Physics, 123, 173–206.

Porrenga, D.H. (1965) Chamosite in recent sediments of the Niger and Orinoco Deltas. Geological Magazine, 44, 400–403.

Putnis, A. (2009) Mineral replacement reactions. Reviews in Mineralogy and Geochemistry, 70, 87–124.

Putnis, A., and Putnis, C.V. (2007) The mechanism of reequilibration of solids in the presence of a fluid phase. Journal of Solid State Chemistry, 180, 1783–1786.

Sheldon, N.D., and Retallack, G.J. (2003) Low oxygen levels in earliest Triassic soils: Comment and reply. Geology, 30, 919–922.

Sillitoe, R.H. (2010) Porphyry copper systems. Economic Geology, 105, 3–41.

Slack, J.F., Jiang, W.T., Peacor, D.R., and Okita, P. (1992) Hydrothermal and metamorphic berthierine from the Kidd Creek volcanogenic massive sulfide deposit, Timmins, Ontario. Canadian Mineralogist, 30, 1127–1142.

Taylor, K.G. (1990) Berthierine from the non-marine wealden (early cretaceous) sediments of south-east England. Clay Minerals, 25, 391–399.

Toth, T.A., and Fritz, S.J. (1997) An Fe-berthierine from a cretaceous laterite: part i. characterization. Clays and Clay Minerals, 45, 564–579.

van Aken, P.A., and Liebscher, B. (2002) Quantification of ferrous/ferric ratios in minerals: New evaluation schemes of Fe L_{23} electron energy-loss near-edge spectra. Physics and Chemistry of Minerals, 29, 188–200.

van Aken, P.A., Liebscher, B., and Styrsa, V.J. (1998) Quantitative determination of iron oxidation states in minerals using Fe L23 - edge electron energy-loss near-edge structure spectroscopy. Physics and Chemistry of Minerals, 25, 323–327.

Van Houten, F.B., and Purucker, M.E. (1984) Glauconitic peloids and chamositic ooids - Favorable factors, constraints, and problems. Earth-Science Reviews, 20, 211–243.

Varga, R.J., Bailey, R.A., and Suemnicht, G.A. (1990) Evidence for 600 year-old basalt and magma mixing at Inyo Craters volcanic Chain, Long Valley Caldera, California. Journal of Geophysical Research, 95, 441–450.

Veblen, D.R. (1983) Microstructures and mixed layering in intergrown wonesite, chlorite, talc, biotite, and kaolinite. American Mineralogist, 68, 566–580.

Veblen, D.R., and Ferry, J.M. (1983) A TEM study of the biotite-chlorite reaction and comparison with petrologic observations. American Mineralogist, 68, 1160–1168.

Wilson, J., Cressey, G., Cressey, B., Cuadros, J., Ragnarsdottir, K.V., Savage, D., and Shibata, M. (2006) The effect of iron on montmorillonite stability. (II) Experimental investigation. Geochimica et Cosmochimica Acta, 70, 323–336.

Wise, M.A. (2007) Crystallization of "pocket" berthierine from the Pulsifer granitic pegmatite, Poland, Maine, USA. Clays and Clay Minerals, 55, 583–592.

Xi, J.X., Yang, Y.P., Ma, L.Y., He, H.P., Xu, H.F., Zhu, J.X., and Wei, J.M. (2022) The composition and growth mechanism of coexisting 4M2 and 4A8 biotite polytypes from rhyolite of Long Valley Caldera, California. Clays and Clay Minerals, 70, 48–61.

514 Xiao, B., and Chen, H.Y. (2020) Elemental behavior during chlorite alteration: New
515 insights from a combined EMPA and LA-ICP-MS study in porphyry Cu
516 systems. Chemical Geology, 543, 1–12.

517 Xu, H.F. (1993) Transmission electron microscopy study of the nonperiodic structures
518 in silicate minerals (Ph.D. dissertation). Johns Hopkins University, Baltimore
519 Maryland.

520 Xu, H.F. (2000) Using electron energy-loss spectroscopy (EELS) associated with
521 transmission electron microscopy to determine oxidation states of Ce and Fe in
522 minerals. Geological Journal of China Universities, 6, 137–144.

523 Xu, H.F., and Veblen, D.R. (1996) Interstratification and other reaction
524 microstructures in the chlorite-berthierine series. Contributions to Mineralogy
525 and Petrology, 124, 291–301.

526 Xu, H.F., and Veblen, D.R. (1996) Interstratification and other reaction
527 microstructures in the chlorite-berthierine series. Contributions to Mineralogy
528 and Petrology, 124, 291–301.

529 Xu, H.F., Jin, S.Y., and Noll, B.C. (2016) Incommensurate density modulation in a
530 Na-rich plagioclase feldspar: Z-contrast imaging and single-crystal X-ray
531 diffraction study. Acta Crystallographica Section B, Structural Science, Crystal
532 Engineering and Materials, 72, 904–915.

533 Xu, H.F., Shen, Z.Z., and Konishi, H. (2015) Natural occurrence of monoclinic Fe_3S_4
534 nano-precipitates in pyrrhotite from the Sudbury ore deposit: A Z-contrast
535 imaging and density functional theory study. Mineralogical Magazine, 79, 377–
536 385.

537 Xu, H.F., Shen, Z.Z., Konishi, H., and Luo, G.F. (2014) Crystal structure of
538 Guinier-Preston zones in orthopyroxene: Z-contrast imaging and ab inito study.
539 American Mineralogist, 99, 2043–2048.

Xu, H.F., Zhang, Y., and Veblen, D.R. (1996) Periodic and nonperiodic interstratification in the chlorite-biotite series. American Mineralogist, 81, 1396–1404.

Yanagisawa, K., Rendón-Angeles, J.C., Ishiwara N., and Oishi, S. (1999) Topotaxial replacement of chlorapatite by hydroxyapatite during hydrothermal ion exchange. American Mineralogist, 84, 1861–1869.

Yang, Y.P., He, H.P., Tan, W., Tao, Q., Yao, J.M., Xian, H.Y., Li, S.Y., Xi, J.X., Zhu, J.X., and Xu, H.F. (2022a) Incorporation of incompatible trace elements into molybdenite: Layered PbS precipitates within molybdenite. American Mineralogist, 107, 54–64.

Yang, Y.P., He, H.P., Xian, H.Y., Xi, J.X., Wu, X., Chen, A.Q., Zhu, J.X., and Xu, H.F. (2022b) Periodic and non-periodic stacking in molybdenite (MoS2) revealed by STEM. American Mineralogist, 107, 997–1006.

Figure Captions

FIGURE 1. Geological map of the Long Valley Caldera, located in California, USA (modified after Bailey, 1976; and Christensen and Depaolo, 1993). The sampling place is indicated by the yellow star.

FIGURE 2. Optical images of rhyolite from Long Valley, California, USA, with an accessory plate (550 nm retardation) inserted. Phenocrysts including **(a)** biotite (Bio), titanomagnetite (Mt), potassium feldspar (Kfs), and **(b)** kaersutite (Krs) are surrounded by xenomorphic plagioclase (Pl).

FIGURE 3. BSE images of biotite particles and focused ion beam (FIB) - sampled position. The associated minerals are kaersutite (Krs) in **(a)** and titanomagnetite (Mt) in **(b)**. The main inclusions in biotite particles are titanomagnetite (Mt) and apatite (Ap) in **(b)** and zircon (Zrn) in **(c)**, respectively. **(d)** A biotite particle with a length of over

250 μm and a width of over 200 μm. **(e)** Enlarged image of the red square in (d), showing the FIB area (marked by the yellow square).

FIGURE 4. STEM images of the biotite FIB section. (a) STEM image of the FIB section. A crack separates the biotite (left side of the section) from plagioclase (right side of the section). The inset figure shows the selected-area electron diffraction pattern of the 1*M* polytype along the [110] axis zone, derived from biotite. **(b)** Enlarged TEM image of the biotite and crack in (**a**), as indicated by the red square, displaying the edge of the biotite section with fracture and secondary clay minerals having curved morphology. **(c)** Enlarged STEM image of the square c in (**b**), showing numerous defects in the host biotite. The yellow and red arrows in (b) and (c) indicate typical defects with higher and lower contrast relative to biotite, respectively.

FIGURE 5. TEM images and the corresponding diffraction (FFT) pattern of biotite. (a) The TEM image shows distinct contrast regions, in which the yellow arrows point to defective domains. Regions with different contrasts are separated by defects, as shown by the A, B, and C regions in biotite that have a high contrast, low contrast, and medium contrast, respectively. **(b)** Enlarged image of the area marked by the red dotted square in (**a**). The arrows indicate two stacking faults with a disordered atomic arrangement. The local FFT pattern of the defect area shows a 1*M* polytype of biotite with a streak feature in $k \neq 3n$ rows.

FIGURE 6. STEM image and energy-dispersive spectroscopy (EDS) results of biotite. (a) Z-contrast STEM image of the biotite domain with dense defects. Black arrows mark the domains with a lower contrast while the white arrows denote the domains with a higher contrast. **(b, c)** EDS spectra collected from two representative areas with different defect densities in (**a**), of which square 1 shows a relatively higher contrast while square 2 displays a lower contrast in comparison to a biotite region. The horizontal lines for comparison show that the intensities of O and Si peaks in (**b**) and (**c**) are almost equal to each other, while the intensities of K, Mg, Al, and particularly Fe peaks in (**b**) are higher than those in (**c**).

FIGURE 7. EELS spectra of the biotite domains with lattice defects, Fe mapping and the ELNES-edge structure at the Fe $L_{3,2}$-edges. (a) TEM image of biotite with defects. The yellow square was investigated via EELS; **(b)** Fe mapping of the studied area based on the EELS result; **(c)** spectra collected from the red squares 1 and 2 in (**b**). The spectra reveal different shapes and peak positions of the Fe-edge between squares 1 and 2.

FIGURE 8. Two-dimensional STEM images of biotite. (a) STEM image of biotite with Fe-rich and Fe-poor domains marked by white and black arrows, respectively. **(b)** High-resolution STEM image of the red square b in (**a**), revealing the co-existence of 1*M*-polytype biotite domains with a lattice spacing of ~10 Å and defect layers with a lattice spacing of ~24 Å (i.e., 10 Å + 4 Å + 10 Å). The yellow arrows that connect the octahedral cations of adjacent layers show the consistent stacking sequence of the defective domains with the host biotite domains. **(c)** Structural diagram of the interstratified domains marked by the red square in (**b**); the pink triangles represent Mg^{2+} in the octahedral sheet (O), purple triangles represent Fe^{2+} in the O sheet, green triangles represent Fe^{3+} in the O sheet, and yellow balls represent interlayer K cations. The brighter lines (or transverse extending spots) are O sheets, the darker spots adjacent to O sheets are tetrahedral sheets (T), and the bright spots between two TOT units of biotite are interlayer K^{+} columns.

FIGURE 9. (HR)STEM images showing adjacent interstratified layers and corresponding atomic arrangement of the host biotite and the twin layers of berthierine. (a) STEM image revealing twin centrosymmetric-like crystals within the two pairs of interstratified domains. **(b)** Enlarged HAADF– STEM image of the squared region in (**a**). **(c)** TOT-type layers of biotite, with Mg^{2+} and Fe^{3+} (and vacancies) as the dominant octahedral cations. **(d)** Interstratified–twin layers of berthierine (marked by the red arrows). These layers with a trioctahedral TO-type structure are Fe^{2+}-rich. **(e)** TOT-O structure of chlorite. The definitions of the symbols in the structural diagram **(c–e)** of the interstratified domains are the same as in Fig. 8.

FIGURE 10. STEM image of defect termination, showing the transformation

623 **from one normal biotite layer to the twin layers of berthierine.** The red square in **(a)**
624 reveals an extra octahedral sheet inserted into the TOT structure of the biotite. The
625 yellow arrow denotes a dislocation line. Transformation process of the biotite layer into
626 two berthierine layers in (**a**), as illustrated by the diagram in **(b)**.

627 **FIGURE 11. Schematic models illustrating the formation mechanism of the**
628 **interstratified berthierine layers. (a)** Deformation, microcleavage, and dislocation in
629 the host biotite, which might serve as fluid channels and initial alteration sites. **(b)**
630 Alteration takes place with an increase of Fe^{3+} content in the biotite layers, resulting in
631 the replacement of interlay K^{+} by newly formed octahedral sheets. Different structural
632 adjustments lead to the formation of two different types of berthierine-related structures
633 **(c)** and **(d)**, as displayed in Figs. 8 and 9, respectively. The definitions of the symbols in
634 the structural diagram of the interstratified domains are the same as in Fig. 8.

FIGURE 1

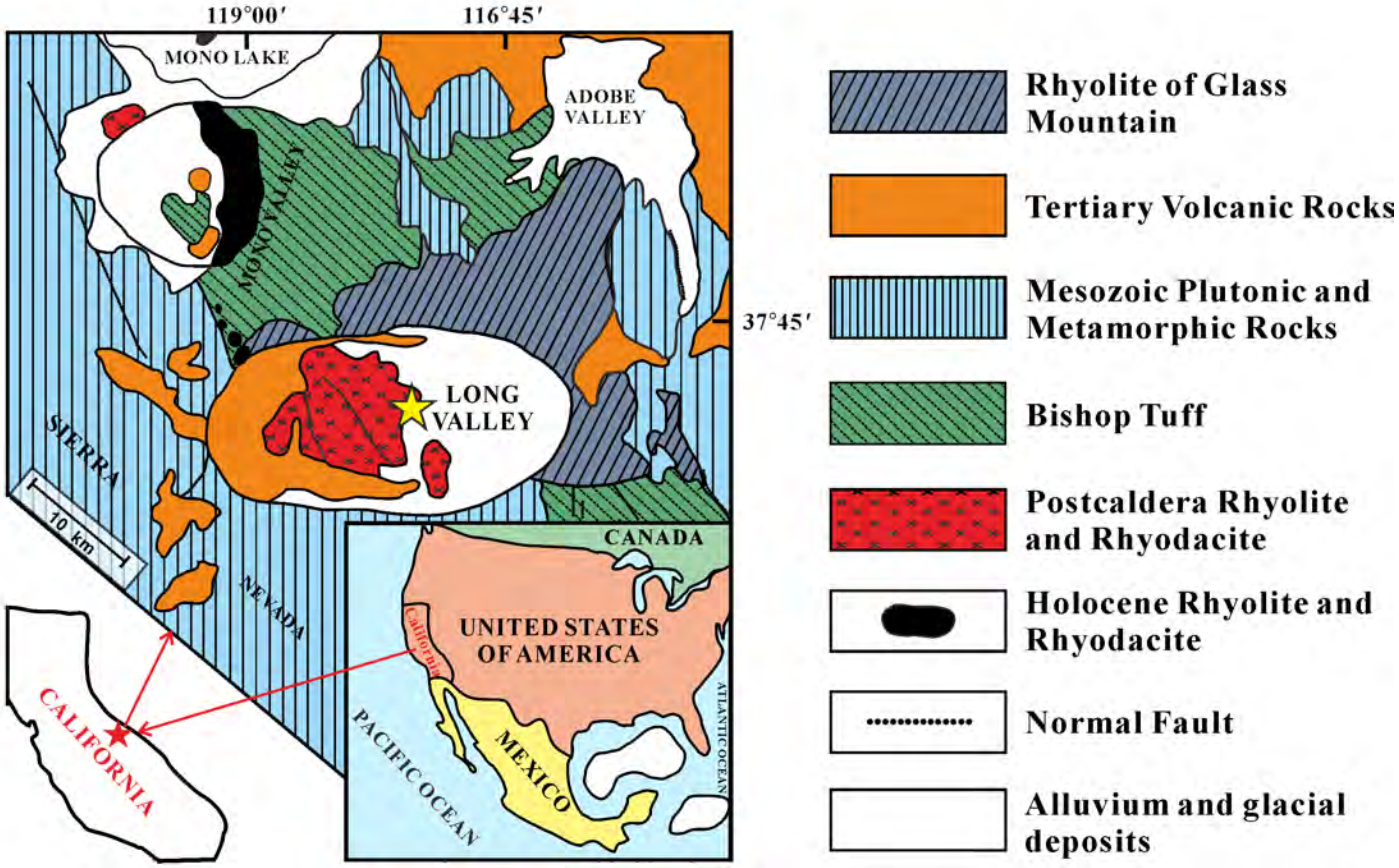

FIGURE 2

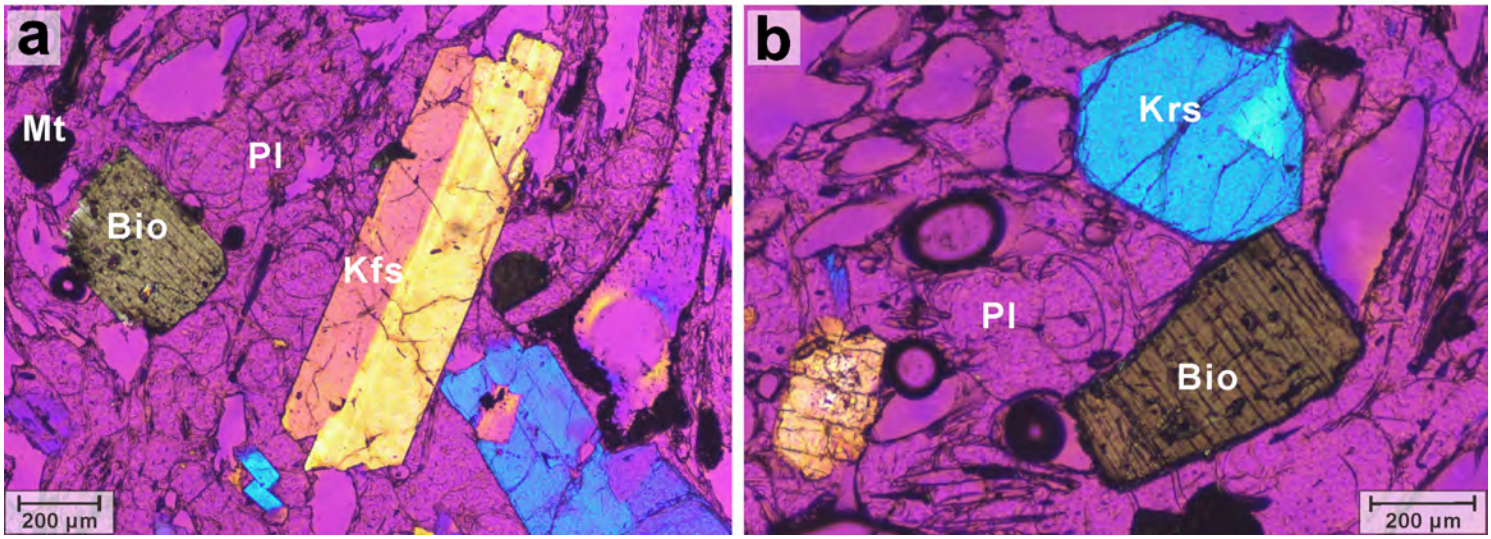

FIGURE 3

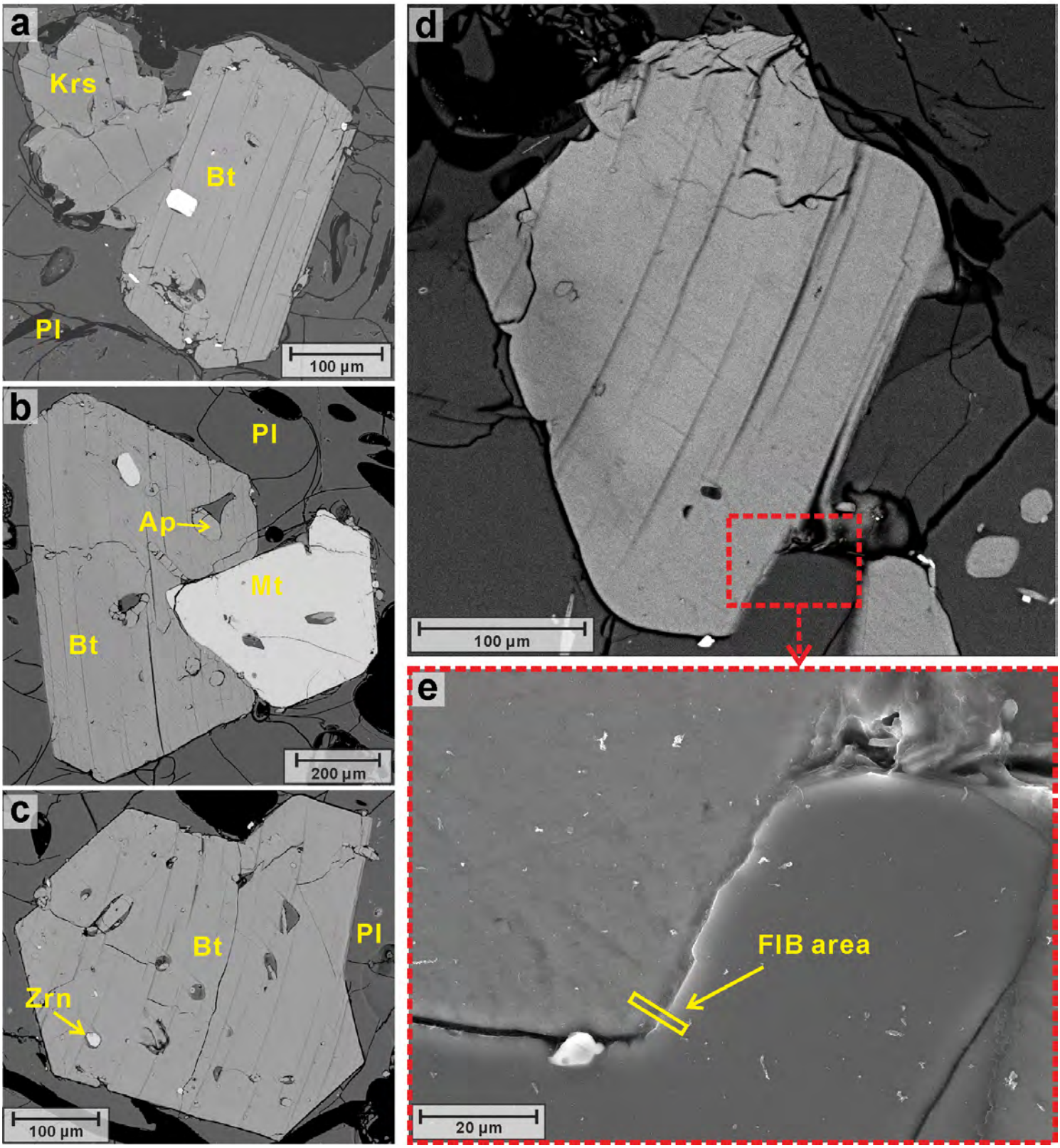

This is the peer-reviewed, final accepted version for American Mineralogist, published by the Mineralogical Society of America.
The published version is subject to change. Cite as Authors (Year) Title. American Mineralogist, in press.
DOI: https://doi.org/10.2138/am-2023-8984. http://www.minsocam.org/

FIGURE 4

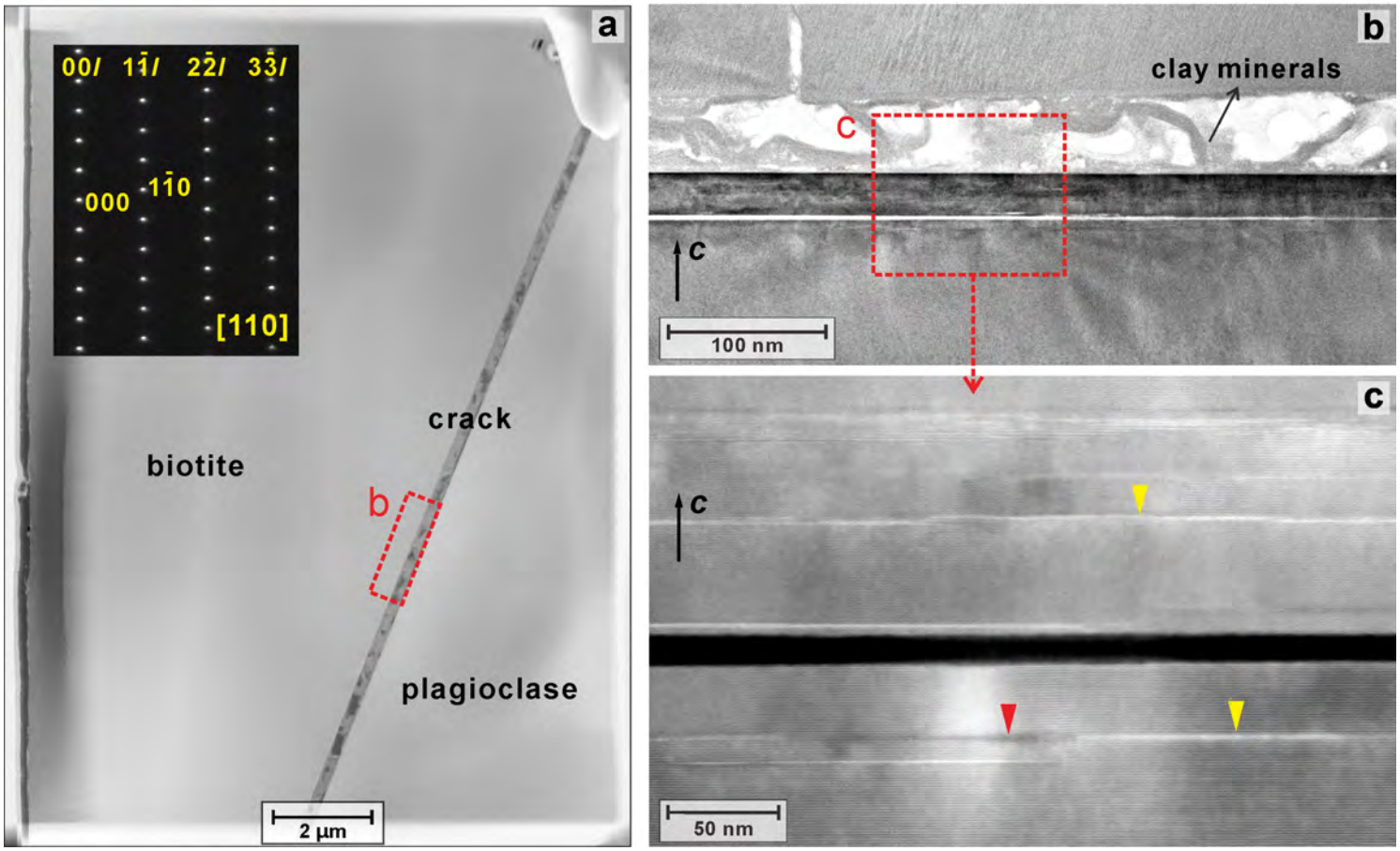

This is the peer-reviewed, final accepted version for American Mineralogist, published by the Mineralogical Society of America.
The published version is subject to change. Cite as Authors (Year) Title. American Mineralogist, in press.
DOI: https://doi.org/10.2138/am-2023-8984. http://www.minsocam.org/

FIGURE 5

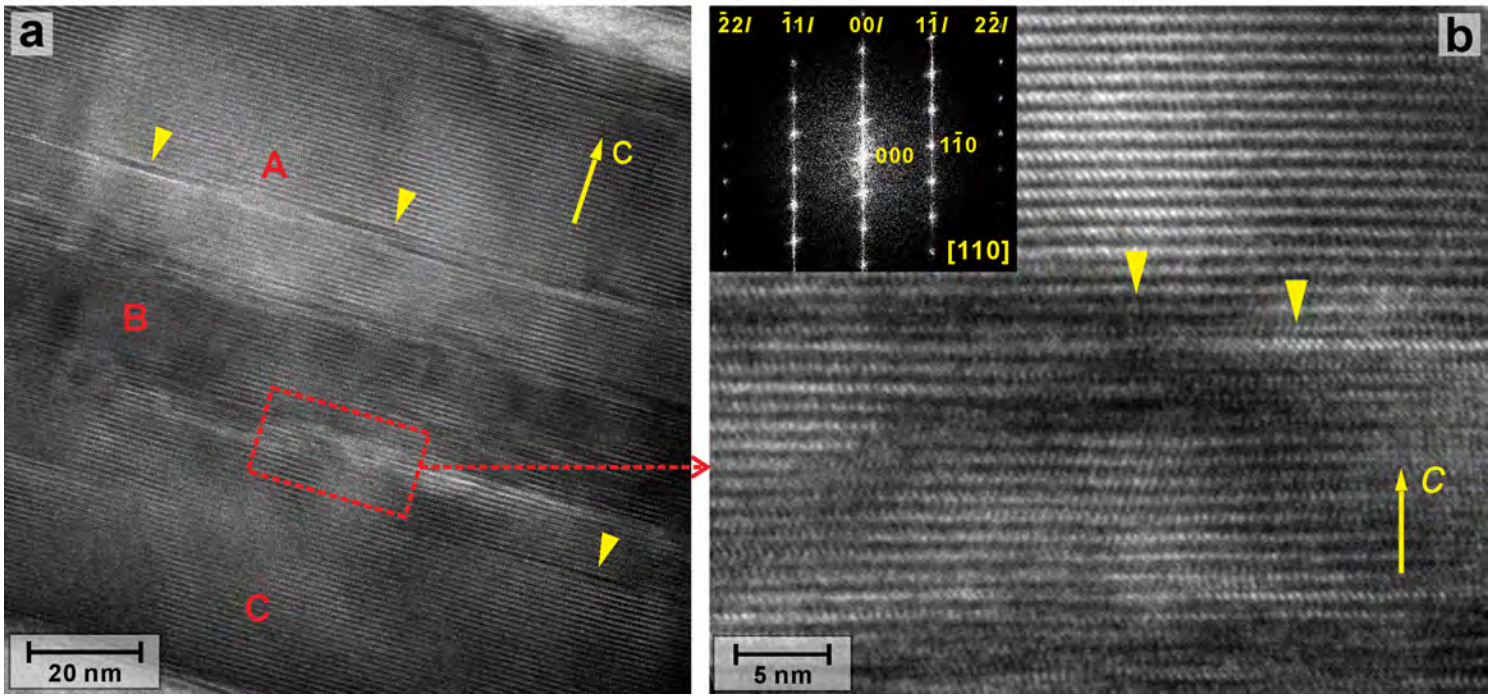

This is the peer-reviewed, final accepted version for American Mineralogist, published by the Mineralogical Society of America.
The published version is subject to change. Cite as Authors (Year) Title. American Mineralogist, in press.
DOI: https://doi.org/10.2138/am-2023-8984. http://www.minsocam.org/

FIGURE 6

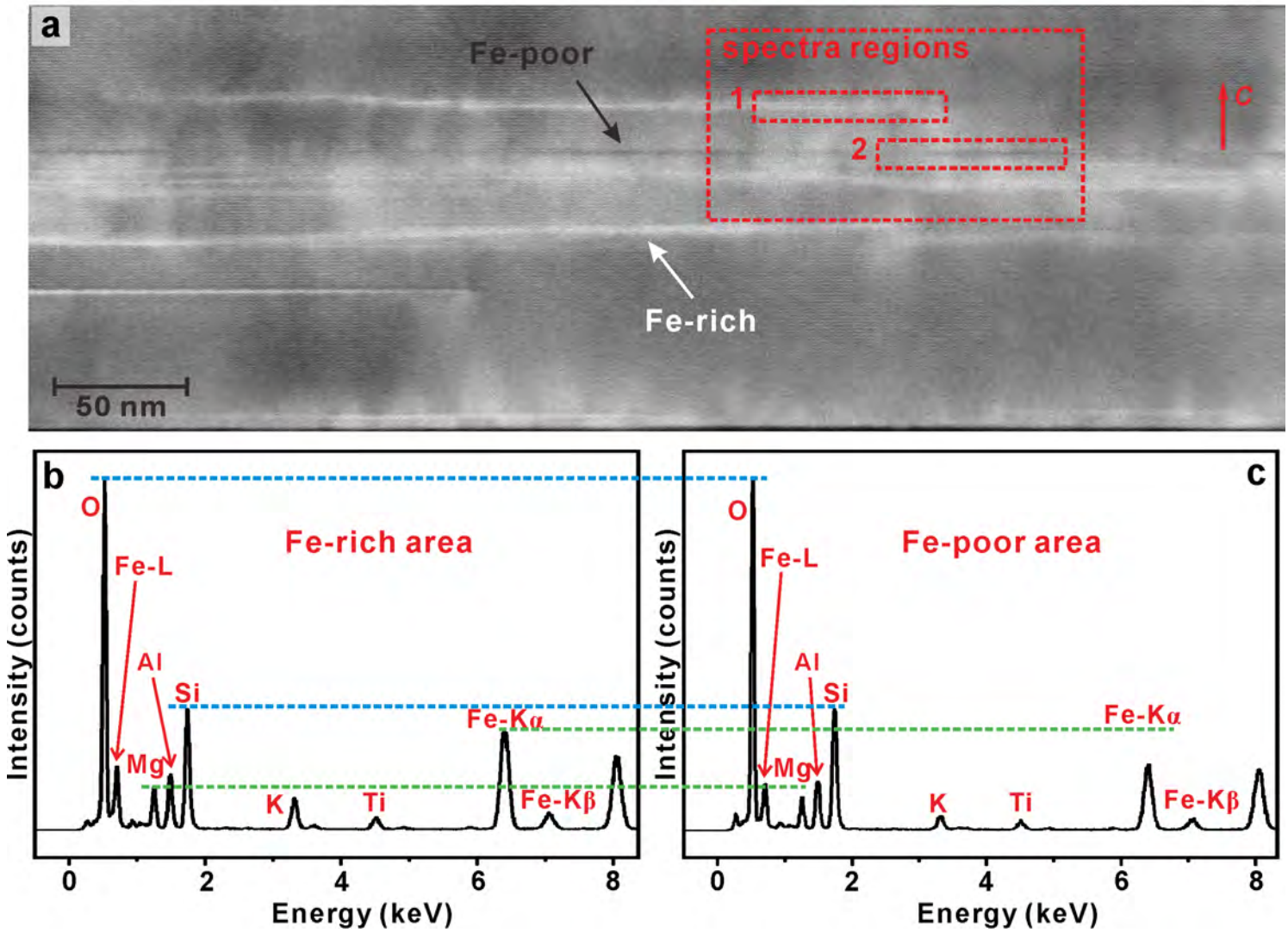

This is the peer-reviewed, final accepted version for American Mineralogist, published by the Mineralogical Society of America.
The published version is subject to change. Cite as Authors (Year) Title. American Mineralogist, in press.
DOI: https://doi.org/10.2138/am-2023-8984. http://www.minsocam.org/

FIGURE 7

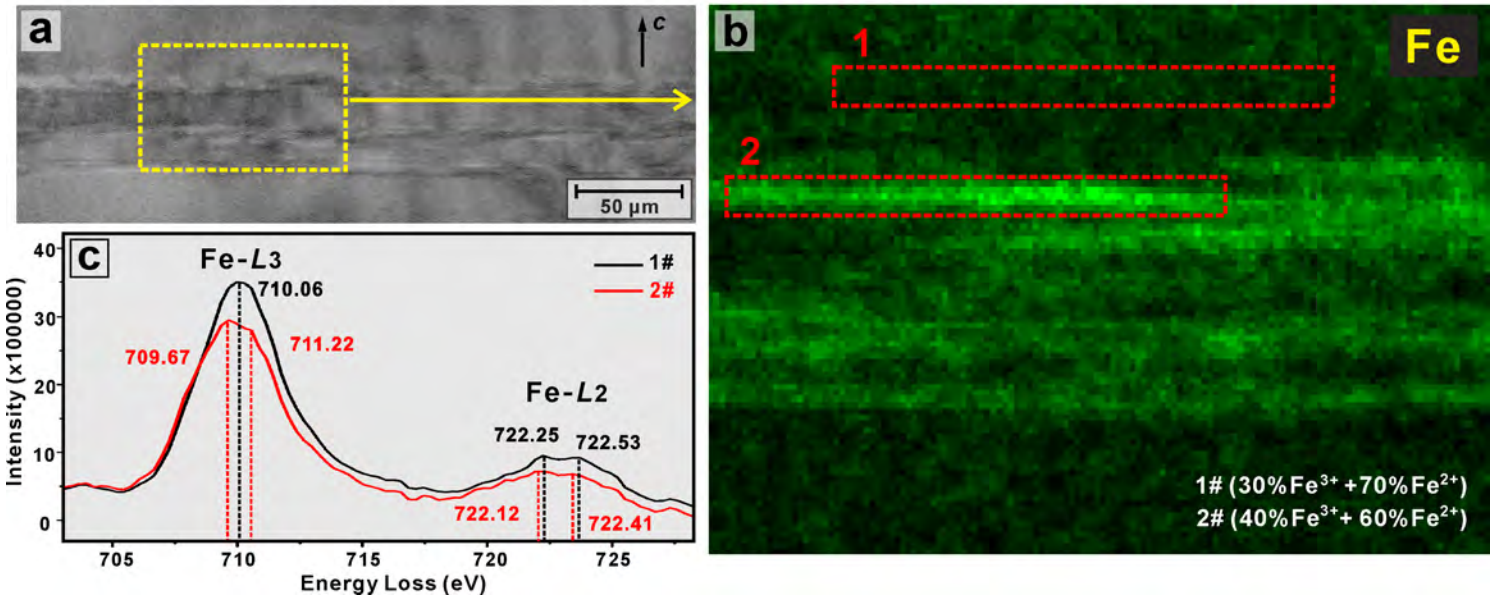

This is the peer-reviewed, final accepted version for American Mineralogist, published by the Mineralogical Society of America.
The published version is subject to change. Cite as Authors (Year) Title. American Mineralogist, in press.
DOI: https://doi.org/10.2138/am-2023-8984. http://www.minsocam.org/

FIGURE 8

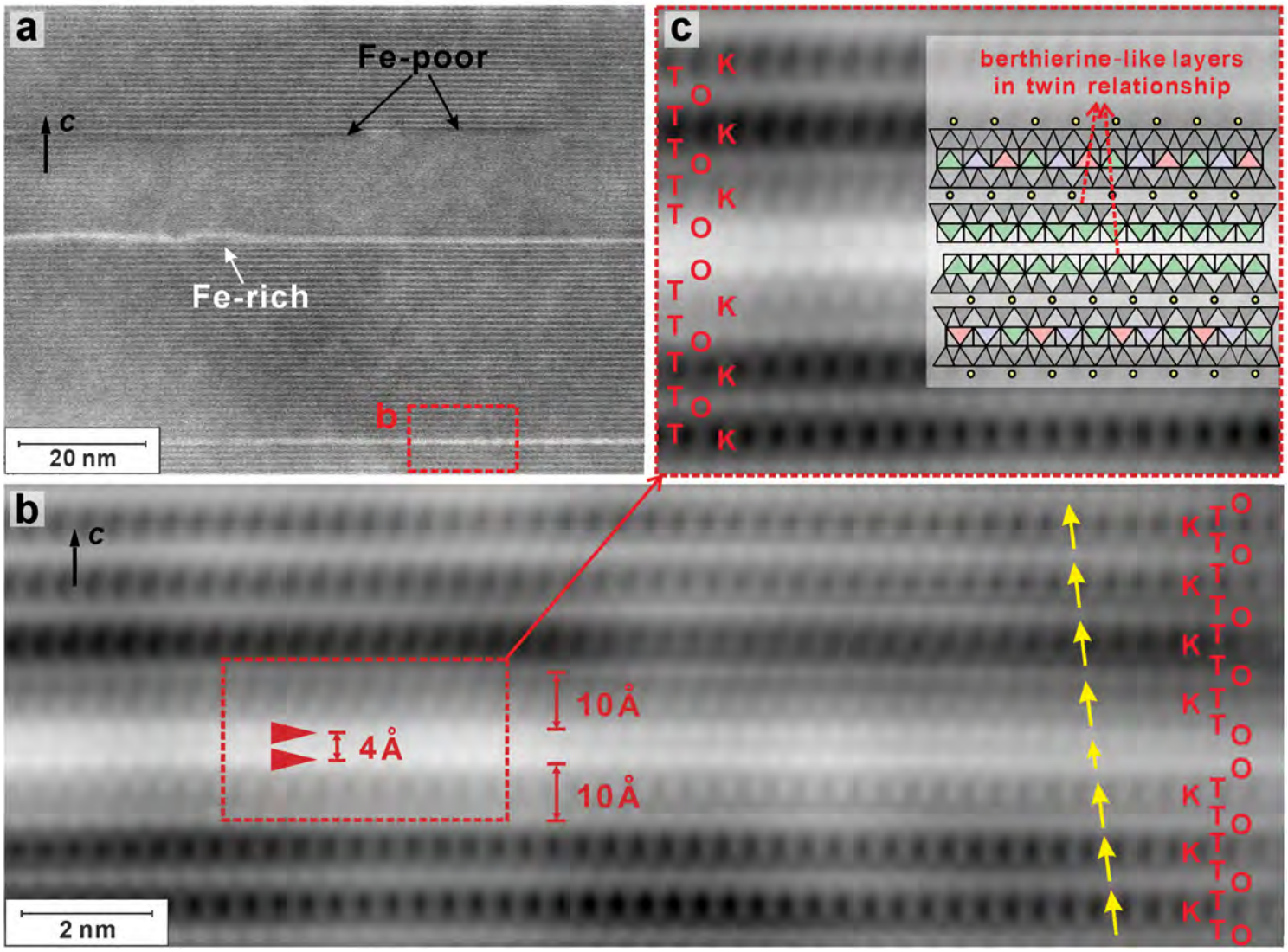

This is the peer-reviewed, final accepted version for American Mineralogist, published by the Mineralogical Society of America.
The published version is subject to change. Cite as Authors (Year) Title. American Mineralogist, in press.
DOI: https://doi.org/10.2138/am-2023-8984. http://www.minsocam.org/

FIGURE 9

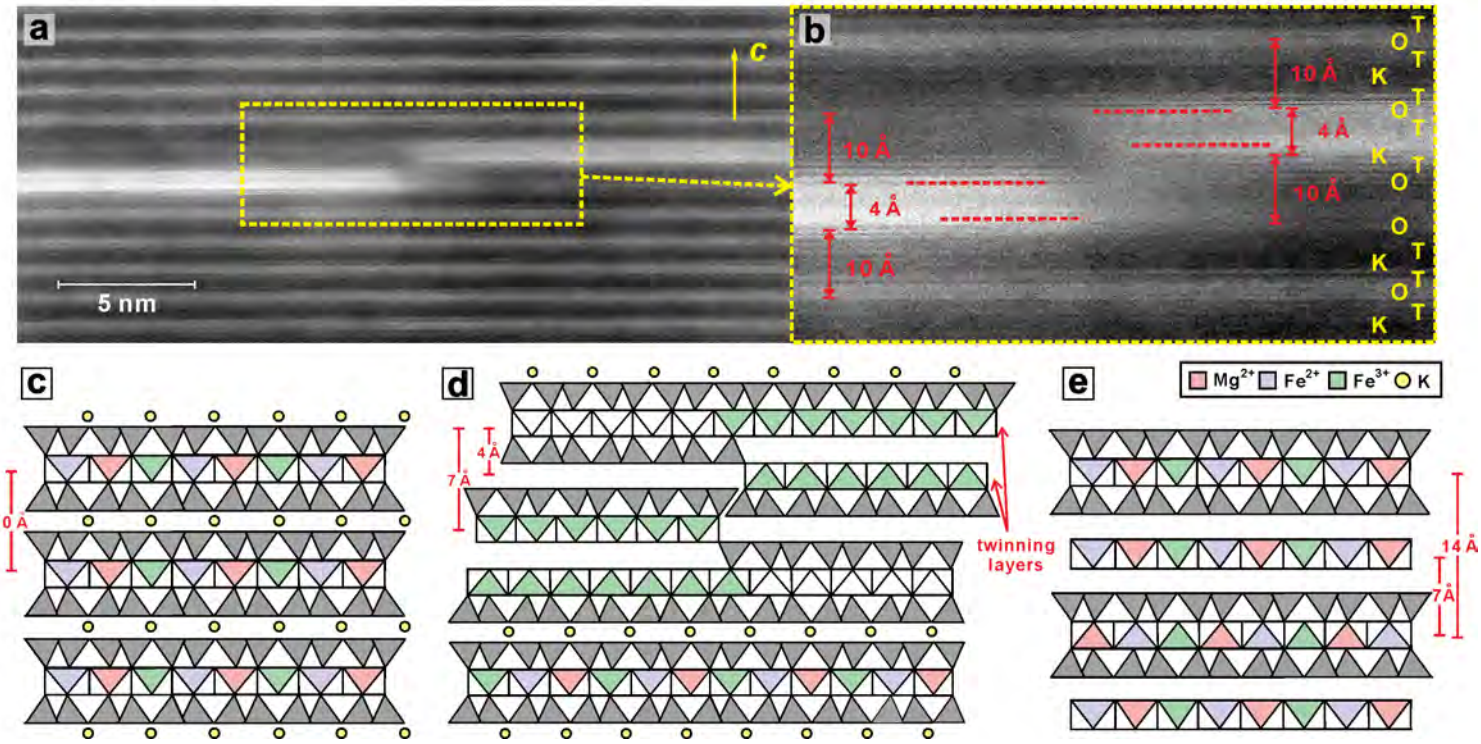

This is the peer-reviewed, final accepted version for American Mineralogist, published by the Mineralogical Society of America.
The published version is subject to change. Cite as Authors (Year) Title. American Mineralogist, in press.
DOI: https://doi.org/10.2138/am-2023-8984. http://www.minsocam.org/

FIGURE 10

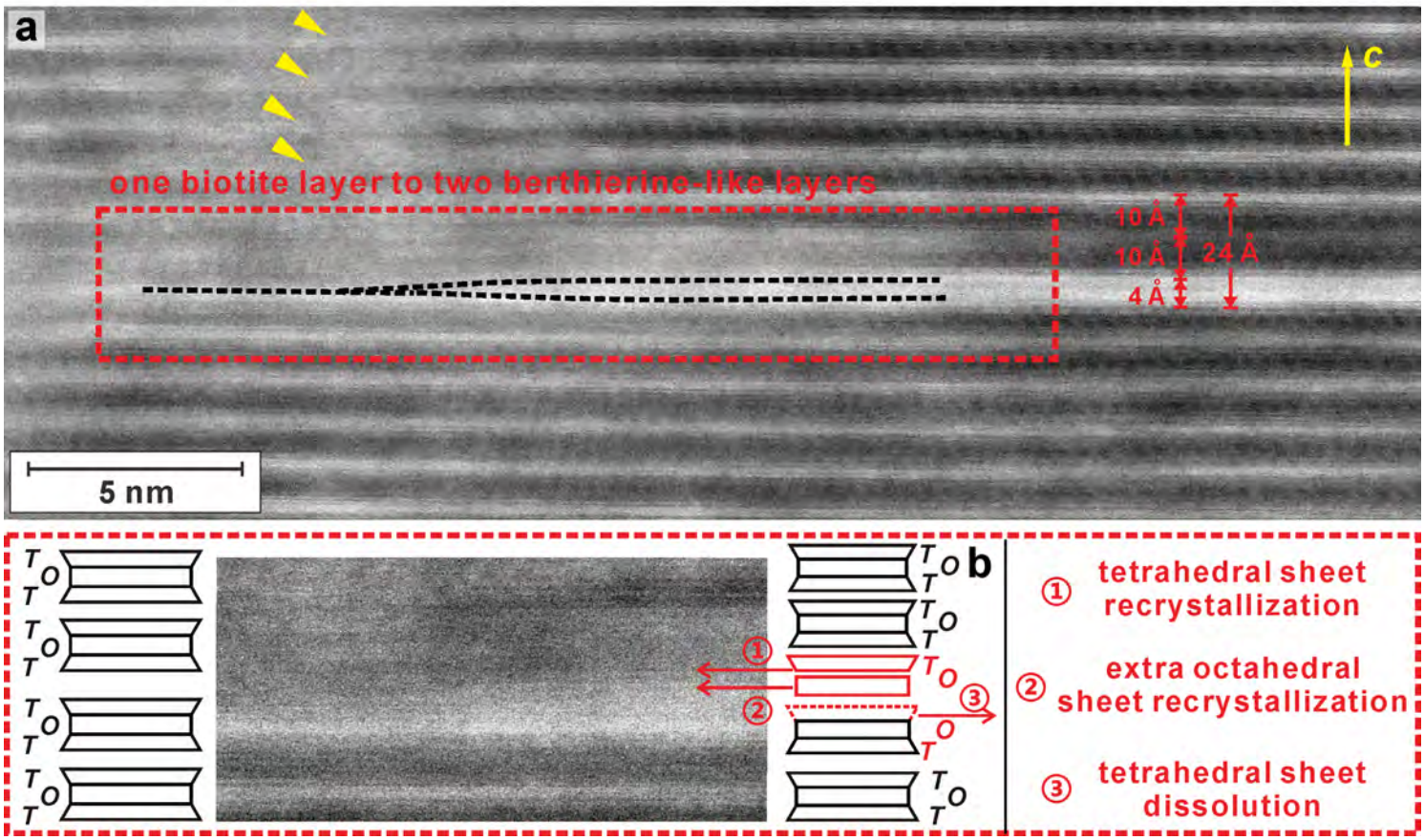

This is the peer-reviewed, final accepted version for American Mineralogist, published by the Mineralogical Society of America.
The published version is subject to change. Cite as Authors (Year) Title. American Mineralogist, in press.
DOI: https://doi.org/10.2138/am-2023-8984. http://www.minsocam.org/

FIGURE 11